Check for updates

Received: 30 March 2023 | Revised: 2 May 2023 | Accepted: 16 May 2023

DOI: 10.1002/jbio.202300105

REVIEW

JOURNAL OF BIOPHOTONICS

Emerging clinical applications in oncology for non-invasive multi- and hyperspectral imaging of cell and tissue autofluorescence

Jared M. Campbell[1,2] | **Abbas Habibalahi**[1,2] | **Shannon Handley**[1,2] | **Adnan Agha**[1,2] | **Saabah B. Mahbub**[1,2] | **Ayad G. Anwer**[1,2] | **Ewa M. Goldys**[1,2]

[1]Graduate School of Biomedical Engineering, University of New South Wales, Sydney, New South Wales, Australia

[2]Australian Research Council Centre of Excellence for Nanoscale BioPhotonics, The University of Adelaide, Adelaide, South Australia, Australia

Correspondence
Jared M. Campbell, Graduate School of Biomedical Engineering, University of New South Wales, Sydney, NSW 2052, Australia.
Email: j.campbell@unsw.edu.au

Funding information
Australian Research Council, Grant/Award Number: DP210102960

Abstract

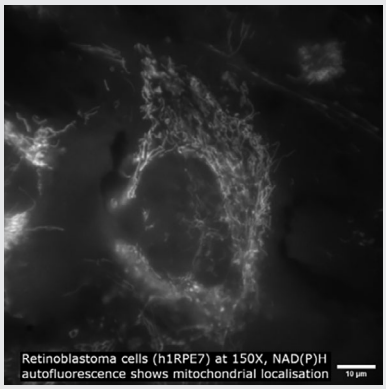

Hyperspectral and multispectral imaging of cell and tissue autofluorescence is an emerging technology in which fluorescence imaging is applied to biological materials across multiple spectral channels. This produces a stack of images where each matched pixel contains information about the sample's spectral properties at that location. This allows precise collection of molecularly specific data from a broad range of native fluorophores. Importantly, complex information, directly reflective of biological status, is collected without staining and tissues can be characterised in situ, without biopsy. For oncology, this can spare the collection of biopsies from sensitive regions and enable accurate tumour mapping. For in vivo tumour analysis, the greatest focus has been on oral cancer, whereas for ex vivo assessment head-and-neck cancers along with colon cancer have been the most studied, followed by oral and eye cancer. This review details the scope and progress of research undertaken towards clinical translation in oncology.

KEYWORDS

autofluorescence, hyperspectral, multispectral, surgical imaging, tumour characterization, tumour margin

1 | INTRODUCTION

The characterisation of cells and tissues in oncology may be undertaken for a wide variety of reasons, notably for tumour diagnosis and monitoring, disease prognosis, and surgical margin definition. Conventional diagnostic methods, for example, non-invasive radiological imaging, or tissue sampling via surgical access, are often not sufficiently informative for optimal clinical decision making [1, 2]. Additionally, they can require the use of exogenous

This is an open access article under the terms of the Creative Commons Attribution License, which permits use, distribution and reproduction in any medium, provided the original work is properly cited.
© 2023 The Authors. *Journal of Biophotonics* published by Wiley-VCH GmbH.

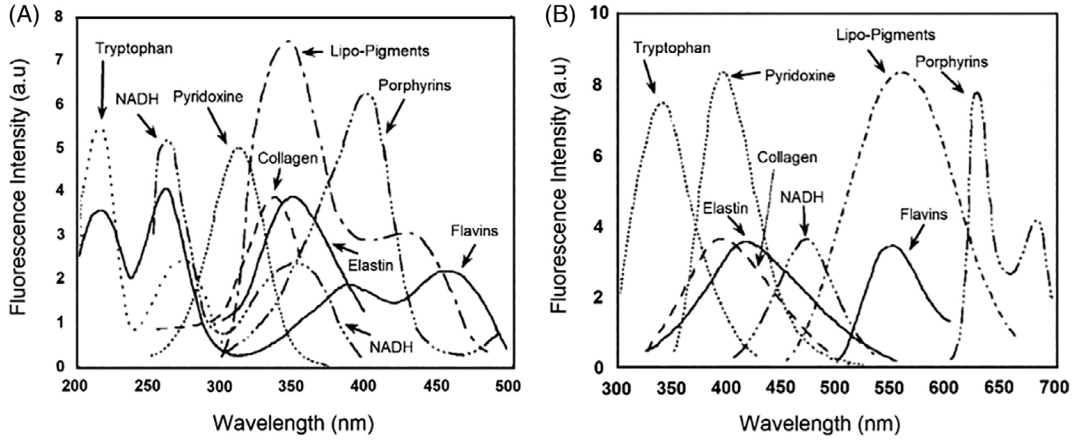

FIGURE 1 (A) Excitation and (B) emission spectra of endogenous tissue fluorophores, adapted with permission from Wagnieres et al. [9].

agents (e.g., radiographic contrast agents, 5-aminolevulinic acid) which can have drawbacks or contraindications, or the collection of tissue biopsies, which, depending on context, may have diagnostic limitations or lead to negative patient outcomes [3–5]. As such, there is a clinical demand for genuinely label free, non-invasive methods of assessment for cells and tissues, able to non-invasively provide the complex biochemical information needed for tumour characterisation and mapping.

Assessment of the native fluorescence of endogenous fluorophores—autofluorescence imaging—has received growing attention as a potential solution to this challenge. Numerous metabolites exist that can be excited to emit light at specific, sometimes uniquely characteristic wavelength ranges [6, 7]. Although often regarded as interfering noise in bioimaging technologies that rely on tagging molecules of interest with fluorescent markers, autofluorescence directly reflects cell and tissue biochemistry and metabolic changes without biopsy, fluorescence probe staining or fixation. Amongst the most prevalent autofluorophores are key indicators of cellular metabolism and its redox state, reduced nicotinamide adenine dinucleotide (NADH) and flavin adenine dinucleotide (FAD), whose relative concentrations give the optical redox ratio [8]. NADH and FAD are the principal electron donors and acceptors of oxidative phosphorylation, respectively. NADH has excitation maxima at 290 and 351 nm and emission maxima at 440 and 460 nm, while FAD has a single excitation maximum at 450 nm with its corresponding emission maxima at 535 nm [9] (Figure 1). Other related endogenous fluorophores, such as NADPH and other members of the flavin family, have sufficiently similar excitation/emission profiles that they are not spectrally distinct from NADH and FAD, but differences in their decay rate (assessable by fluorescence-lifetime imaging microscopy (FLIM) [10]) can allow them to be discriminated if needed.

By imaging the same area with a series of different excitation and/or emission combinations (channels) it is possible to obtain spectral profiles of the cells or tissue under examination. This imaging strategy is termed multi or hyperspectral imaging—depending on the number of channels ultimately utilised—multispectral imaging generally refers to a small number of bands (e.g., 3–10) while hyperspectral images have more bands (up to hundreds, typically with much narrower spectral bandwidth). Here, these terms are used interchangeably. The hyperspectral/multispectral images can then be mapped to the characteristics of known autofluorophores with greater precision than techniques that only target select key wavelengths of individual autofluorophores [7, 11–13]. In this process, adjustments typically need to be made for background fluorescence [14, 15] from other autofluorophores.

Hyper- and multispectral imaging quantify autofluorescent molecules at a single pixel level, making it possible to produce spatial maps of these informative disease markers in cells and tissues [7, 11, 16]. In hyper and multispectral imaging, every pixel is characterised by its own spectral profile reflecting the distributions of fluorophores. The hyper- and multispectral imaging data sets contain spatial and molecular information which can be assessed through Big Data-driven modern image analysis methodologies for the direct prediction of highly informative cell and tissue characteristics [17, 18]. The spectral and spatial features extracted via image analytics provide an additional dimension of assessment than standard spectrometry without image information [19]. Importantly, hyper- and multispectral imaging of autofluorescence can yield non-invasive methodologies for rapid assessment [20], requiring very limited amounts of sample, down to the single cell level [21]. Some of these use single-photon fluorescence which has low-cost instrumentation whereas two-photon autofluorescence

18640648, 0, Downloaded from https://onlinelibrary.wiley.com/doi/10.1002/jbio.202300105 by University of Adelaide Alumni, Wiley Online Library on [20/06/2023]. See the Terms and Conditions (https://onlinelibrary.wiley.com/terms-and-conditions) on Wiley Online Library for rules of use; OA articles are governed by the applicable Creative Commons License

requires specialised instrumentation and highly trained personnel [22, 23].

Beyond all other conditions, research attention has been focused on the application of hyper and multispectral imaging of cell autofluorescence to oncology. The native fluorescence from cancerous tissue/cells has been utilised to examine their physiological processes and changes at the cellular level. Changes in the metabolic environment of cells (e.g., normal vs. cancer cells, changes after treatment) can be explored through the fluorescence spectra and abundance of fluorophores. Endogenous fluorophores including NADH, NADPH, FAD and porphyrins have generally been explored to analyse metabolic changes [24, 25], whereas elastin [26] and collagen have been used to look at structural changes [27].

The metabolic profile between healthy cells and cancer cells differs due to their varying genetics and metabolic microenvironment. Tumours create a hypoxic environment where oxygen levels are approximately 1%–2% lower compared to healthy tissue [28]. In this case, glycolysis is the main form of ATP production compared to oxidative phosphorylation in normal cells. In glycolysis, the cellular redox status changes where NAD^+ is reduced to NADH. It also supports the pentose phosphate pathway (PPP), aiding in the production of NADPH [29]. Consequently, this increase in production of NADH and NADPH is important for cancer cells to maintain metabolic homeostasis [29].

The changes in metabolism in cancerous and non-cancerous tissue have been studied by analysing the fluorescence spectra of fluorophores [24, 25]. NADH and FAD are the main coenzymes involved in cellular metabolism and are generally the predominate fluorescent signals present, thus are often used as metabolic markers [30]. Dramicanin et al. found increased NADH concentration in malignant breast tissue, suggesting that this was due to damaged mitochondrial metabolism and a shift to anaerobic metabolism [25]. They also found an increase in intensity of PpIX in the malignant tissue, due to the tissue having better vascularity [25]. Similar results were found by Pu et al. who observed an increase in NADH and FAD content in breast tissue compared to normal tissue, however, there was a decrease in collagen [24]. The main fluorophore in the ECM of breast tissue is type 1 collagen. For cancerous tissue to metastasise, they degrade the ECM, consequently leading to the loss of collagen [31, 32]. Therefore, by analysing the fluorescent intensity/profile of these autofluorophores, biochemical and physiological information can be collected.

Tryptophan is another autofluorophore that has been studied in cancer research. Tryptophans are amino acids and are important for protein synthesis. Zhang et al. found a higher concentration of tryptophan in MDA-MB-231 breast cancer cells compared to MCF-7 (non-aggressive breast cancer cells) or normal fibroblast cells [33]. Cancer cells are known to take up more tryptophan as there have larger amino acid transporters on the cell membrane, thus leads to the suppression of the immune response against the cancer cells [33].

As such it has been clear from the earliest stages of research on endogenous fluorescence that there was great potential to address the major oncological priorities of accuracy in detection (minimising false negative results which result in treatment delay and false positives which can cause further invasive testing and unnecessary therapy) as well as speed of tissue characterisation (intra-operative assessment being extremely valuable and rapid diagnoses improving treatment planning and sparing patients potentially unnecessary periods of stress).

In this review, we explore all potential clinical applications of hyper and multispectral imaging of cell and tissue autofluorescence that have been investigated for the field of oncology, and summarise the evidence currently supporting their translation.

2 | HYPER AND MULTISPECTRAL AUTOFLUORESCENCE IN ONCOLOGY

A scoping review strategy [34] was employed to identify all contemporary studies on hyper and multispectral imaging of autofluorescence with a focus on addressing an oncologic, clinical issue. We utilised title, key and indexing terms (e.g., multispectral, hyperspectral, spectral, multi-modal, endogenous fluorescence, native fluorescence, autofluorescence) joined by Boolean operators in Pubmed, Scopus, and Embase, from 2010 to September 2021. An initial 3307 potential studies were identified, which was reduced to 213 on review of the titles and abstracts with a final 32 studies included after consideration of the full texts. These showed that studies have been carried out for multiple forms of cancer, with diverse applications considered. The approaches taken and resulting findings of these studies are detailed in this review to provide an overview of the field and inform future research and translation.

Cancers that have been investigated using hyper/multispectral imaging include colon [35–39], oral [40–48], head and neck [49–53], skin [54, 55], breast [56, 57], cervical [58], gastric [59], ocular [17, 20], bladder [60], lung [61], brain [62, 63], and ovarian [64] (Table 1). Research interest in this area is intensifying, with seven publications published 4 years covered by this scoping review, eight in the second, and 16 in the most recent.

18640648, 0, Downloaded from https://onlinelibrary.wiley.com/doi/10.1002/jbio.202300105 by University of Adelaide Alumni, Wiley Online Library on [20/06/2023]. See the Terms and Conditions (https://onlinelibrary.wiley.com/terms-and-conditions) on Wiley Online Library for rules of use; OA articles are governed by the applicable Creative Commons License

TABLE 1 Clinical applications of hyperspectral imaging of autofluorescence to cancer.

	Excitation	Emission	Single or two photon	Context	Finding
Cancer (in vivo)					
Oral					
(Roblyer, Kurachi et al. 2010) [40]	365, 380, 405 and 450 nm	18 emission features based on RGB colour channels	Single	Surgical microscope; non-neoplastic, dysplastic and cancerous oral tissue. Detection.	Sensitivity 100% Specificity 85% for discriminating dysplasia/cancer samples from non-neoplastic samples
(Jo, Cheng et al. 2018) [41]	355 nm	390 ± 20, 452 ± 22.5, >500 nm	Single	Handheld FLIM endoscope; mild-dysplasia, early stage oral cancer, benign lesions. Detection and delineation.	Sensitivity >90%, Specificity >85%, ROC-AUC >0.9, Negative predictive value 98% for diagnosis
(Lu, Wang et al. 2018) [42]	455 nm	500–720 in 5 nm steps	Single	CRI Maestro; oral neoplasia (mouse tongue model). Detection.	Regions of tongue neoplasia were defined with ex vivo AUC 0.87 ± 0.03, in vivo AUC 0.84 ± 0.06. Accuracies for normal, dysplasia, carcinoma in situ and squamous cell carcinoma were 75%, 76%, 83% and 91%
(Pal, Edward et al. 2017) [43]	780 nm	400–650 nm	Two	Multiphoton microscopy system with incorporated spectrometer; DMBA hamster model of oral pre-cancer and OSCC. Characterisation.	Control and neoplastic tissue samples characterised. The intensity of a PpIX peak and its ratio with a blue–green peak were significantly different in control and neoplastic tissues.
(Duran-Sierra, Cheng et al. 2020) [44]	355 nm	390 ± 20 nm, 452 ± 22.5 nm, >500 nm	Single	FLIM endoscopy; precancerous and cancerous oral lesions. Characterisation.	Several autofluorescent features were significantly different between precancerous/cancerous oral lesions and normal oral tissue.
(Bedard, Schwarz et al. 2013) [45]	405 nm	471–667 nm	Single	Snapshot imaging spectrometer; lesions and clinically normal sites in oral cancer patients. Characterisation.	Lesions had decreased overall, blue/green and red wavelength intensities.
Skin					
(Romano, Teixeira Rosa et al. 2020) [54]	355 nm	390 ± 20, 452 ± 22, >496 nm	Single	FLIM dermoscopy system with handheld probe; patients with diagnosed nodular BCC lesions, normal regions. Detection.	Statistical classifiers from FLIM features discriminated BCC from healthy tissue with ROC = 0.82
(Lihachev, Derjabo et al. 2015) [55]	405 nm	Red and green spectral bands	Single	Samsung Galaxy Note 3 phone camera; skin neoplasms from BCC patients and an atypical nevus patient. Characterisation.	BCC cases had lower autofluorescence in malignant tissue compared with healthy skin. In all BCC cases, the Normalized intensity decrease maps had high-intensity decrease rates at the tumour areas with low intensity in comparison with healthy skin and the internal ulcerating area.

18640648, 0, Downloaded from https://onlinelibrary.wiley.com/doi/10.1002/jbio.202300105 by University of Adelaide Alumni, Wiley Online Library on [20/06/2023]. See the Terms and Conditions (https://onlinelibrary.wiley.com/terms-and-conditions) on Wiley Online Library for rules of use; OA articles are governed by the applicable Creative Commons License

TABLE 1 (Continued)

	Excitation	Emission	Single or two photon	Context	Finding
Cervical					
(Bae, Lee et al. 2016) [58]	638 nm	Visible spectral range and 700 nm	Single	Animal scope; tumorigenic cells grafted into the thighs of nude mice. Characterisation.	NADH and flavin autofluorescence as background to PpIX highlighted tumours
Cancer (ex vivo)					
Head and neck					
(Halicek, Dormer et al. 2020) [49]	455 nm	500–720 nm in 10 nm increments	Single	Cri Maestro; specimens from patients undergoing resection of thyroid tumours or salivary gland tumours. Detections	All thyroid tumours AUC = 0.85 ± 0.2; papillary thyroid carcinoma AUC = 0.81 ± 0.03; medullary and insular thyroid carcinomas AUC = 0.86 ± 0.06; follicular adenoma and carcinoma AUC = 0.95 ± 0.02; poorly differentiated carcinoma AUC = 0.98 ± 0.01. Parotid salivary tumours AUC = 0.60 ± 0.30; other salivary tumours AUC = 0.80 ± 0.14.
(Halicek, Dormer et al. 2019) [50]	455 nm	500–720 nm in 10 nm increments	Single	Maestro spectral imaging system; specimens from patients undergoing head and neck SCC resection. Delineation.	Conventional SCC; AUC = 0.93 for discriminating tumour only from normal only, for HPV positive SCC AUC = 0.86.
(Fei, Guolan et al. 2017) [52]	455 nm	450–950 nm	Single	Maestro imaging camera; surgical tissue specimens of head and neck cancer patients. Delineation.	In the oral cavity, normal tissues discriminated from cancerous tissue AUC = 0.83 ± 0.1; in the thyroid gland AUC = 0.74 ± 0.33
(Lu, Little et al. 2017) [53]	455 nm	450–950 with 2 nm increments	Single	Maestro imaging system; surgical tissue specimens from head and neck cancer surgery. Delineation.	Cancer from normal tissue in the: oral cavity AUC = 0.82 ± 0.20 thyroid gland AUC = 0.72 ± 0.31; larynx and pharynx AUC = 0.74 ± 0.26 paranasal and nasal AUC = 0.81 ± 0.11
(Shah and Skala 2015) [51]	750, 890 nm	440/80, 550/100. 450/35 nm	Single	Inverted multiphoton microscope and time-correlated single photon counting electronics; ex vivo tissue from head and neck cancer patients. Characterisation.	Adenocarcinoma tissue had higher redox ratios and lower NADH and FAD fluorescence lifetimes than to squamous cell carcinoma
Oral					
(Yan, Huang et al. 2017) [46]	365, 405 nm	490–590, 590–690, 650–750 nm	Single	Portable LED-Induced Autofluorescence multispectral imager; normal and tumour regions in resected oral squamous carcinoma. Discrimination.	Normal tissue discriminated from tumour regions with sensitivity = 84.68%, specificity = 76.24% accuracy = 80.66%

(Continues)

18640648, 0, Downloaded from https://onlinelibrary.wiley.com/doi/10.1002/jbio.202300105 by University of Adelaide Alumni, Wiley Online Library on [20/06/2023]. See the Terms and Conditions (https://onlinelibrary.wiley.com/terms-and-conditions) on Wiley Online Library for rules of use; OA articles are governed by the applicable Creative Commons License

TABLE 1 (Continued)

	Excitation	Emission	Single or two photon	Context	Finding
(Yan, Cheng et al. 2021) [47]	365, 405 nm	470, 505, 525, 532, 550, 595, 632, 635, 695 nm	Single	Portable LED-Induced Autofluorescence multispectral imager; tissue from patients with suspicious oral lesions. Discrimination.	Normal tissue discriminated from tumour regions with sensitivity = 96.15%, specificity = 69.55%, and accuracy = 82.85%.
(Duann, Jan et al. 2013) [48]	330–385, and 470–490 nm	400–1000 nm	Single	Regular inverted microscope; keratinized tissues from oral cancer patients. Characterisation.	Independent component analysis resolved more reliable spectral fingerprints for keratinized tissues for all oral cancer tissue sections than principal component analysis.
Colon					
(Deal, Mayes et al. 2018) [35]	360–550 in 5 nm increments	378/16, 402/16, 449/15, 501/15, 561/14 nm	Single	Custom inverted microscope; Normal and neoplastic tissue from resected human colon sections. Characterisation.	Neoplastic to normal ratio for elastin was <1 for 8 of the 9 patients; NADH >1 for 6 of the 9 patients.
(Banerjee, Rial et al. 2013) [36]	260–650 nm	340–650 nm	Single	Prototype wide-field spectral imager; normal mucosa, polypoid and flat adenomas, adenocarcinoma from surgical colon specimens. Delineation	Dividing image intensity of tryptophan with the image intensities of FAD and collagen achieved superior contrast for visualising colonic neoplasms.
(Banerjee, Renkoski et al. 2012) [37]	260–650 nm	340–650 nm	Single	Prototype multispectral imaging system; surgical specimens of colonic neoplasms and normal mucosa after resection. Characterisation.	Peak emissions, from cancer cells for spectra consistent with tryptophan were twice that of normal cells.
(Meyer, Stella et al. 2020) [38]	785 nm	425–650 in 10 nm increments	Two	Custom-built multi-photon microscope; cancerous and normal epithelial colon cells cultivated to form spheroids. Discrimination.	31.5% improvement in discrimination compared to values from published literature.
(Kim, Lew et al. 2021) [39]	375 nm	420–700 in ~20 nm steps	Single	An endoscopic system with four imaging modalities; fresh-frozen tissues from colon cancer patients. Delineation.	Normal compared to cancerous tissue: sensitivity = 0.86, and specificity = 0.85.
Brain					
(Poulon, Chalumeau et al. 2018) [62]	275 nm, 690–1040 nm	Tyrosine, tryptophan, collagen, NADH	Single	Intraoperative optical probe for optical biopsy; fixed biopsy tissues of primary (glioblastoma), secondary (metastasis) tumour and control cortex. Delineation.	Tyrosine-tryptophan, tryptophan-collagen, and tryptophan-NADH ratios achieved 90% sensitivity, 73% specificity. NADH-FAD and Porphyrin-NADH ratios achieved 97% sensitivity and 100% specificity.

18640648, 0, Downloaded from https://onlinelibrary.wiley.com/doi/10.1002/jbio.202300105 by University of Adelaide Alumni, Wiley Online Library on [20/06/2023]. See the Terms and Conditions (https://onlinelibrary.wiley.com/terms-and-conditions) on Wiley Online Library for rules of use; OA articles are governed by the applicable Creative Commons License

TABLE 1 (Continued)

	Excitation	Emission	Single or two photon	Context	Finding
(Poulon, Pallud et al. 2018) [63]	890 nm	380–780 nm in 10 nm steps	Two	Multimodal two-photon microscope; freshly extracted normal, glioblastoma, and brain metastasis from adult patients. Delineation.	NADH/FAD, fitted SHG intensity and average lifetime achieved 100% sensitivity and 50% specificity.
Breast					
(Carver, Locknar et al. 2019) [56]	375, 405 and 488 nm	Spectrometer with 10 emission bins	Single	Multispectral confocal scanning system; fresh, ex-vivo, surgical specimens. Delineation.	NADH and FAD concentrations were definably different between cancer and a benign condition fibroadenoma.
(Keller, Majumder et al. 2010) [57]	340 nm	400–720 nm	Single	Portable spectroscopic system; samples from total or partial mastectomies	Negative and positive margins delineated with sensitivity = 85% specificity = 96% specificity.
Eye					
(Habibalahi, Bala et al. 2019) [17]	340, 368, 373, 378, 382, 388, 391, 394, 405, 413, 432, 441, 455, 460, 470, 491, 510 ± 5 nm	420–460, 454–496, 573–613, 575–650 nm	Single	Custom-made wide-field fluorescence microscopy system; formalin-fixed, paraffin-embedded OSSN in tissue biopsies. Delineation.	Pixel-wise correlation between histology assessment and multispectral analysis of ∼78% for inter-patient classification and ∼94% for intra-patient classification.
(Habibalahi, Allende et al. 2019) [20]	340, 368, 373, 378, 382, 388, 391, 394, 405, 413, 432, 441, 455, 460, 470, 491, 510 ± 5 nm	420–460, 454–496, 573–613, 575–650 nm	Single	Custom-made wide-field fluorescence microscopy system; formalin-fixed, paraffin-embedded OSSN in tissue biopsies. Delineation.	OSSN detected with 1% and 14% misclassification errors.
Gastric					
(Li, Xie et al. 2019) [59]	361 nm	450–680 in 2 nm increments	Single	Hyperspectral microscopy imaging system; patients diagnosed with non-atrophic gastritis, premalignant lesions or gastric cancer. Discrimination.	Accuracy, specificity and sensitivity >94%.
Bladder					
(Pradère, Poulon et al. 2018) [60]	870 nm	380–780 in 10 nm steps	Two	Multimodal two-photon microscope; fixed samples of healthy and cancerous urothelium. Characterisation.	Significant differences in intensities for high and low-grade tumours. Redox ratio higher in healthy tissue than tumour, and low grade higher redox ratio than high.

(Continues)

18640648, 0, Downloaded from https://onlinelibrary.wiley.com/doi/10.1002/jbio.202300105 by University of Adelaide Alumni, Wiley Online Library on [20/06/2023]. See the Terms and Conditions (https://onlinelibrary.wiley.com/terms-and-conditions) on Wiley Online Library for rules of use; OA articles are governed by the applicable Creative Commons License

TABLE 1 (Continued)

	Excitation	Emission	Single or two photon	Context	Finding
Lung					
(Kilin, Mas et al. 2017) [61]	720 nm	400–650 nm in 10 nm increments	Two	Laser-induced autofluorescence microscopy system; three-dimensional in vitro model of lung cancer. Characterisation.	Non-cancerous tissue had two times the autofluorescence intensity of cancerous, with decay in the direction of the main tumour body.
Ovarian					
(Renkoski, Hatch et al. 2012) [64]	365 nm	400–600 nm	Single	Wide field spectral imager; freshly resected human ovaries. Discrimination.	Normal and cancerous ovaries discriminated; sensitivity = 100% sensitivity, specificity = 51%. Specificity increased to 69% by dividing autofluorescence data with green reflectance values.

Note: Detection = studies with a focus on the detection or grading of neoplasia at the lesion level (potential application to screening or diagnosis); Delineation = studies with a focus on defining tumour regions within tissue (potential application to the definition of surgical margins); Characterisation = Studies with a focus on investigating the properties of neoplastic tissues without applying those findings to differentiation.

It is readily apparent that work has focused on accessible tumours that can be reached endoscopically (e.g., colon and oral) or external tumours (e.g., ocular and skin). This is unsurprising as this optical imaging technology is best suited for application in areas of the body which do not require surgery to access. As such, it is meaningful to consider studies in terms of which were applied to live tumours still in the body (in vivo; Section 3) and which assessed excised and surgical specimens (in vitro; Section 4).

3 | IN VIVO ASSESSMENT OF CANCER

The characterisation of tissues by autofluorescence can be carried out non-invasively, without necessitating its removal for processing and histology staining. As such, one of the key areas of interest for the application of multi and hyperspectral microscopy to oncology has been cancer screening. Many forms of cancer diagnosis involve the invasive collection of biopsies, which creates a difficult balance for clinicians who must judge when suspicious tissue warrants further investigation.

3.1 | Oral cancer

Oral cancers, which have good accessibility for in vivo assessment and screening have received significant attention for the application of hyperspectral imaging of autofluorescence. Early research by Roblyer et al. [40] used a surgical microscope for the assessment of non-neoplastic, dysplastic and cancerous oral tissue. Excitation was at 365, 380, 405 and 450 nm (each with ~50 nm bandwidth) and 18 emission features were obtained using colour channels, including the mean values of the red, green, and blue channels as well as the ratio of the mean red-to-green, red-to-blue, and green-to-blue pixel values. They found that excitation at 405 nm gave the best image contrast, and the ratio of red-to-green fluorescence intensity computed from these images provided the best classification of dysplasia/cancer versus non-neoplastic tissue, with a sensitivity of 100% and a specificity of 85% in the validation, although the ability to separate precancerous lesions from cancerous was more limited. Using a multi-spectral FLIM handheld endoscope [41] excited clinically suspicious oral lesions at 355 nm, collecting emission bands at 390 ± 20, 452 ± 22.5, and >500 nm. They were able to diagnose mild dysplasia and early-stage oral cancer with AUC > 0.9. Furthermore, with a negative predictive value (the ratio of true negatives to total negative test results) of 98%, this gives strong support that the multi-spectral assessment of oral lesions could be used to avoid unnecessary biopsies in this region.

In vivo, hyperspectral imaging of autofluorescence (455 nm excitation, 500–720 nm emission) applied to a mouse model of oral cancer, detected tongue neoplasia with an AUC of 0.84 ± 0.06 [42]. Classification of specific neoplastic transformations was also undertaken with accuracies of 75%, 76%, 83% and 91% for normal, dysplasia, carcinoma in situ and squamous cell carcinoma

18640648, 0, Downloaded from https://onlinelibrary.wiley.com/doi/10.1002/jbio.202300105 by University of Adelaide Alumni, Wiley Online Library on [20/06/2023]. See the Terms and Conditions (https://onlinelibrary.wiley.com/terms-and-conditions) on Wiley Online Library for rules of use; OA articles are governed by the applicable Creative Commons License

respectively. In an in vivo study using a hamster model, Pal et al. [43] used multiphoton autofluorescence microspectroscopy (780 nm excitation, emissions collected 400–650 nm) to characterise oral epithelial squamous cell carcinoma (OSCC). A red shift of a blue–green (480–520 nm) peak and a prominent peak for OSCC and some high-grade dysplasia at 635 nm (which was attributed to PpIX) were observed. The fluorescence intensity of the PpIX peak and the ratio of this peak and the blue–green peak had statistically significant differences between control and neoplastic tissues.

Other works have focused more on the characterisation of neoplastic properties over the development of diagnostic algorithms. Another study of FLIM endoscopy (emission 390 ± 20, 452 ± 22.5, and >500 nm; excitation 355 nm) [44] found several autofluorescent features with statistically significant different distributions between precancerous and cancerous oral lesions and normal oral tissue. While a single device which combined assessment of reflectance and autofluorescence (with an emission range of 471–667 and a 405 nm LED used for excitation) was used to create snapshot images of normal controls and patients with oral cancer [45] and demonstrated that abnormal tissues had autofluorescence spectra with low intensity, relative decreases in blue/green wavelength region and an increase in red wavelength region.

3.2 | Skin cancer

Skin cancers have similarly ready accessibility for in vivo assessment to oral cancers. Fluorescence lifetime imaging (FLIM) dermoscopy was used by Romano et al. [54] with a triple emission band 390 ± 20, 452 ± 22, and >496 nm and excitation at 355 nm to discriminate nodular basal skin carcinoma (BCC) CC from healthy tissue, achieving an AUC of 0.82. Interestingly, in Lihachev et al. [55], the advancing quality of smartphone cameras was exploited to develop a translatable system suitable for remote primary evaluation of suspicious skin lesions. Here skin autofluorescence was assessed at 405 nm excitation, with emissions captured in the red and green spectral bands by a Samsung Galaxy Note 3 smartphone-integrated CMOS RGB image sensor, with BCC shown to have lowered intensity compared to surrounding healthy skin.

3.3 | Cervical cancer

Another in vivo study was carried out in a mouse model of cervical cancer (TC-1 cells transformed with human papillomavirus, injected into the flank) [58]. Here, multispectral imaging—with a 638 ± 3 nm LED and a multiband-pass filter with the visible spectral range tailored to detect NADH and flavin autofluorescence (used for background image) and 700 nm for PpIX—helped to visualise and highlight tumours by distinguishing them from normal areas. This study also found that their system was sensitive to real-time dynamic photochemical reactivity through assessment of PpIX photobleaching, raising its potential application for treatment monitoring.

4 | EX VIVO ASSESSMENT OF CANCER

Despite its advantages for clinical translation applications, the in vivo assessment of tumours can be difficult to achieve, especially for areas less accessible than oral and skin cancers. As such, the majority of research on the application of hyper and multi-spectral assessment of cancer autofluorescence has been carried out ex vivo on tissue biopsies or, in some cases, in vitro cultured cells from neoplastic cell lines. Even here, the accelerated nature of this form of imaging, which does not require periods of fixation and staining, has major potential for guiding surgeries and some of the research has direct potential for translation.

4.1 | Head and neck cancer

One group of authors has published several studies investigating the use of hyperspectral imaging of autofluorescence for assisting surgeries for head and neck cancer. In Halicek et al. [49], they applied their system, which for fluorescence microscopy used a 455 nm excitation source with emissions collected every 10 nm from 500 to 720 nm at 10 nm increments, to the detection of cancer in thyroid and salivary glands using normal tissues, tissue from the primary tumour and tissue from the tumour margin from patients undergoing resection. For thyroid tumours, they obtained AUCs of 0.85 ± 0.2 for all thyroid tumours, 0.81 ± 0.03 for papillary thyroid carcinoma, 0.86 ± 0.06 for medullary and insular thyroid carcinomas, 0.95 ± 0.02 for follicular adenoma And carcinoma, and 0.98 ± 0.01 for poorly differentiated carcinoma. For salivary tumours, AUC was 0.60 ± 0.30 for parotid, and 0.80 ± 0.14 for other tumours. The same system was applied in [50] for the investigation of head and neck squamous cell carcinoma (SCC) margin detection in surgical specimens. For their conventional SCC cohort, inter-patient experiments had a median AUC of 0.93 for discriminating tumour only from normal only, while for HPV-positive SCC the median was 0.86. Their study showed that autofluorescence hyperspectral imaging (and also

18640648, 0, Downloaded from https://onlinelibrary.wiley.com/doi/10.1002/jbio.202300105 by University of Adelaide Alumni, Wiley Online Library on [20/06/2023]. See the Terms and Conditions (https://onlinelibrary.wiley.com/terms-and-conditions) on Wiley Online Library for rules of use; OA articles are governed by the applicable Creative Commons License

reflectance) outperformed fluorescent dye-based imaging methods, with the capacity to accurately detect cancer margins in ex-vivo specimens within minutes.

In two further studies, hyperspectral imaging of autofluorescence was compared to hyperspectral imaging of reflectance [52, 53]. As above, cancers were delineated from normal tissue in fresh surgical specimens of people with head and neck cancer using 455 nm excitation and collecting emissions at 10 nm intervals from 500 to 650 nm [53]. Overall, they obtained AUCs of 0.82 ± 0.20 for oral cavity, 0.72 ± 0.31 for gland, and 0.74 ± 0.26 for larynx and pharynx and 0.81 ± 0.11 for paranasal and nasal. In another study aiming to apply hyperspectral imaging, with autofluorescence contrasted to reflectance for tumour margin assessment in surgical tissue specimens [52], normal tissues were discriminated from cancerous tissue in the oral cavity (AUC $= 0.83 \pm 0.19$) and the thyroid gland (AUC $= 0.74 \pm 0.33$). In both cases, hyperspectral imaging of reflectance was noted to have outperformed autofluorescence.

Using an inverted multiphoton microscope with time-correlated single photon counting (enabling FLIM imaging) a different group investigated hyperspectral imaging of ex vivo head and neck cancer patient tissues and showed that adenocarcinoma tissues had higher redox ratios coupled with lower NADH and FAD fluorescence lifetimes compared to squamous cell carcinoma tissue [51]. NADH signal was isolated with excitation wavelength at 750 nm and a 440/80 nm bandpass emission filter, while FAD signal was isolated with an excitation wavelength at 890 nm and a 550/100 nm bandpass emission filter. Adenocarcinoma samples additionally had higher collagen content than squamous cell carcinoma tissues (identified through second harmonic generation imaging).

4.2 | Oral cancer

In addition to the in vivo studies of multispectral imaging of oral cancer autofluorescence (Section 3.1) several works have also investigated excised tissue sections—generally with a view towards developing the technology towards in vivo application. Two such studies, Yan 2017 and Yan 2021 applied different constructions of their LED-Induced Autofluorescence (LIAF) multispectral imager to ex vivo sections of tissue from oral cancer patients and healthy controls. The first study [46] investigated using 365 or 405 nm excitation and emission filters at 490–590, 590–690 and 650–750 nm to discriminate tissue sections from patients with oral cancer from those without. Optimum discrimination (sensitivity 84.68%, specificity 76.24% and accuracy 80.66%) was achieved by illumination with the 365 nm LED and no filters. In a follow-up study [47], 365 and 405 nm excitation LEDs were applied with emission filters with centre wavelengths at 470, 505, 525, 532, 550, 595, 632, 635, and 695 nm. Single-layer network processing was used to select six classifiers using the 470, 505, 532 and 550 nm emission filters which could predict the presence of oral cancer with a sensitivity 96.15%, specificity 69.55% and accuracy 82.85%. Based on the high sensitivity and non-reliance on expert interpretation the authors concluded that the LIAF multispectral imager would be useful for rapid screening and early detection of oral cancer.

Another study applied independent content analysis to separate spectral mixtures in hyperspectral images of keratinised tissues from oral cancer patients [48]. They used two excitation wavelengths (330–385 and 470–490 nm) with emissions collected by a 'hyperspectrometer' [48] spanning 400–1000 nm, and obtained good correlation coefficients with the known characteristics of autofluorophores (0.92 ± 0.09 and 0.97 ± 0.03, respectively). The authors noted that the detection of keratinised tissue was of no particular diagnostic value for the early diagnosis of cancer (occurring as it does in the later stages), but the study was undertaken as an early pilot of the application of the technology to diagnostics.

4.3 | Colon cancer

Most studies described in this review studied systems with an increased number of emission wavelengths assessed, stimulated by a comparatively limited number of excitation wavelengths. In contrast, Deal et al. used a very broad range of excitation wavelengths (360–550 nm) in 5 nm increments, with a long-pass emission filter and dichroic beamsplitter used to separate excitation and emission light at 550 nm [35]. They demonstrated that their technology was able to separate signals of endogenous fluorophores (collagen, elastin, PpIX, FAD and NADH) in order to detect relative differences in concentrations of fluorophores between normal and neoplastic colon tissue.

The Identification of specific fluorophores as biomarkers in colon cancer was also the focus of a study by Banerjee et al., who undertook hyperspectral imaging with a wide field Xenon-lamp based spectral imager capable of illumination from 260 to 650 nm and detection from 340 to 650 nm [36] to target tryptophan (excitation 280 nm, emission 300–410 nm), collagen (excitation 370 nm, emission 410–500 nm as well as excitation 440 nm, emission 600–680 nm), FAD (excitation 440 nm, emission 500–600 nm). They showed that by dividing the image intensity of tryptophan—pixel by pixel—with the

18640648, 0, Downloaded from https://onlinelibrary.wiley.com/doi/10.1002/jbio.202300105 by University of Adelaide Alumni, Wiley Online Library on [20/06/2023]. See the Terms and Conditions (https://onlinelibrary.wiley.com/terms-and-conditions) on Wiley Online Library for rules of use; OA articles are governed by the applicable Creative Commons License

image intensities of FAD and collagen they achieved superior contrast for enhancing the visibility of colonic neoplasms. This built on work from the same group in colon cancer where they found that hyperspectral imaging with excitation from 260 to 650 nm and emission collection from 340 to 650 nm resulted in cellular emission spectra with a peak at 330–340 nm when excited at 280 nm—consistent with the emission of tryptophan—and that peak emission from cancerous cells was about twice that of normal cells [37]. Meyer et al. investigated the discrimination of 2D cultured cancerous and normal epithelial colon cells by redox ratio using two-photon excited fluorescence (TPEF) and an algorithm for the selection of optimised bandpass filters for the detection of autofluorophores without reliance on prior knowledge of their characteristics [38]. Their hyperspectral multiphoton microscopy system (which applied a 785 nm laser and spectrometer detection of emission) achieved a 31.5% improvement of cancer–non-cancer discrimination compared to the use of previously researched values from published literature.

An endoscopic system which combined four imaging modalities—white light imaging, high-frequency ultrasound brightness-mode imaging, integrated backscattering coefficient (IBC) imaging and also multispectral autofluorescence imaging (375 nm excitation, emission collected 420–700 in ~20 nm steps)—was used to characterise excised colon tissue [39]. The multispectral assessment achieved sensitivity 0.86 and specificity 0.85 for discriminating between normal and cancerous tissue.

4.4 | Brain cancer

Fluorescence-guided surgery is already in common use for brain surgery, typically making use of 5-aminolevulinic acid (5-ALA) stimulation of the accumulation of the autofluorophore PPIX in order to better define tumour margins and optimise the safety of the resection of tumours [65]. A study was undertaken on fixed biopsy tissues of primary (glioblastoma), secondary (metastasis) tumour and control cortex to define biomarkers to aid in the surgical resection of high-grade brain tumours without the administration of exogenous factors [62]. Excitation was performed in deep UV (275 nm) and near infra-red (690–1040 nm) with the detection modalities including fluorescence imaging, spectroscopy and fluorescence lifetime imaging. These were used to define ratios for tyrosine-tryptophan, tryptophan-collagen, and tryptophan-NADH which enabled discrimination with 90% sensitivity and 73% specificity as well as NADH-FAD, and Porphyrin-NADH ratios which enabled 97% sensitivity and 100% specificity. A multiscale algorithm which used the three most effective markers. Porphyrin-NADH ratio, Tryptophan collagen ratio and average lifetime at 890 m separated primary tumours from healthy regions with only 1.8% overlap, secondary tumours and healthy regions with 0% overlap, and primary tumours from secondary tumours with 6.7% overlap. The same group used two photon microscopy to discriminate normal brain tissue from glioblastomas and brain metastasis in fresh biopsies [63]. Excitation at 890 nm with emission measured from 380 to 780 nm in 10 nm steps was used to define used NADH/FAD, fitted SHG intensity and the average lifetime which resulted in 100% sensitivity and 50% specificity.

4.5 | Breast cancer

The real-time detection of breast cancer was investigated by Carvar et al. [56] who created single colour-coded images for the assessment of surgical margins and needle-based biopsies using data cubes with excitations at 375, 405 and 488 nm with 10 spectral bins bounded by two of the emission wavelengths. By assessing cellular concentrations of NADH and FAD they found definable differences between cancer and a benign condition fibroadenoma for which differential diagnosis is needed. These authors built a high-speed set-up which could generate 10 data cubes per second, which was sufficiently rapid to be able directly to monitor surgical margins at the cellular level during lumpectomies. An earlier study investigated the use of autofluorescence (excitation 340 nm, emission detected from 400 to 720 nm) combined with diffuse reflectance spectroscopy to evaluate tumour margins in tissue masses removed during partial mastectomies [57]. They achieved 85% sensitivity and 96% specificity for the classification of negative and positive margins. Additionally, neo-adjuvant chemotherapy-treated and non-treated tissue could be discriminated with 100% accuracy.

4.6 | Eye cancer

Despite its accessibility and the desirability of technology which would minimise the collection of biopsies, relatively little work was found that applied the hyperspectral assessment of autofluorescence to the detection of ocular cancers. Habibalahi et al. investigated ocular surface squamous neoplasia (OSSN) in tissue biopsies and mapped the samples' multispectral profiles to expert histological assessment [17]. They applied a high number of LED excitation wavelengths (340, 368,

18640648, 0, Downloaded from https://onlinelibrary.wiley.com/doi/10.1002/jbio.202300105 by University of Adelaide Alumni, Wiley Online Library on [20/06/2023]. See the Terms and Conditions (https://onlinelibrary.wiley.com/terms-and-conditions) on Wiley Online Library for rules of use; OA articles are governed by the applicable Creative Commons License

373, 378, 382, 388, 391, 394, 405, 413, 432, 441, 455, 460, 470, 491 and 510 ± 5 nm) with emissions collected across filters at 420–460, 454–496, 573–613 and 575–650 nm. They obtained a pixel-wise correlation between histology assessment and multispectral analysis of ∼78% for inter-patient classification and ∼94% for intra-patient classification. As their methodology was fully automated with the potential to produce diagnostic maps rapidly and in quasi-real time, they noted its potential for translation for intraoperative assessment for defining tumour boundaries for OSSN. This was reinforced in a related work where the application of 10 or 5 select channels from their set could detect OSSN with 1% and 14% misclassification errors, decreasing imaging times by 75% and 80%, respectively [20]. In an additional work published since this review's primary search, the same group used a similar technology with 59 channels to automatically discriminate pterygium and/or OSSN from 50 patients from normal tissue with an accuracy of 88%, and also defined boundaries in close agreement with hematoxylin and eosin stained sections [66].

4.7 | Gastric cancer

The potential application of hyperspectral imaging of autofluorescence to the early diagnosis of gastric cancer was studied by Li et al. [59]. Here, samples from patients pathologically diagnosed as non-atrophic gastritis, premalignant lesions or gastric cancer were collected and imaged using hyperspectral technology (361 nm excitation, emission 450–680 nm, collected every 2 nm). They showed that the average spectra of the investigated forms of gastric cancer differed at 496, 546, 640 and 670 nm emission wavelengths. A diagnostic model which used the hyperspectral data achieved accuracy, specificity and sensitivity above 94%, which the authors concluded supported the application of hyperspectral imaging of autofluorescence for the non-invasive, sensitive, real-time diagnosis of early gastric cancer.

4.8 | Bladder cancer

In Pradère et al., the potential of multispectral imaging of autofluorescence for the detection of bladder cancer was investigated using fixed samples of healthy and cancerous urothelium [60]. Excitation was at 870 nm with emission detection covering 380–780 nm in 10 nm steps. Significant differences in intensities of emission were observed for high and low-grade tumours. Further, the calculation of the redox ratio indicated that healthy tissues had a higher ratio compared to tumour samples, and low-grade tumours had higher ratios than high.

4.9 | Lung cancer

Using a three-dimensional in vitro model of lung cancer (reconstructed human epithelium with human lung fibroblasts and lung adenocarcinoma cell lines) a two-photon laser-induced autofluorescence microscopy system (excitation at 720 m, emission 400–650 nm in 10 nm steps) was able to detect differences in spectral and intensity heterogeneity at the edges of tumours [61]. Non-cancerous tissue had twice the intensity of cancerous, with autofluorescence decaying in the direction of the main body of the tumour—indicating potential sensitivity of multispectral assessment of autofluorescence to the impact of tumours on their microenvironment.

4.10 | Ovarian cancer

Renkoski et al. imaged freshly resected human ovaries with excitation at 365 nm and emission collected on eight spectral bands from 400 to 600 nm as a step towards developing a tool for screening for ovarian cancer [64]. Linear discriminant analysis was used to define a model which was able to classify normal and cancerous ovaries with 100% sensitivity and 51% specificity, with specificity being able to be increased to 69% by dividing autofluorescence data with green reflectance values to correct for variations in tissue absorption. The same algorithm classified ovaries with benign neoplasms as non-malignant.

5 | CONCLUSIONS

Hyper and multispectral imaging of autofluorescence has been trialled in vivo and ex vivo for the non-invasive characterisation of neoplastic tissue and suspect lesions. A primary driver of in vivo human translation seems to be tissue accessibility, as the non-invasive nature of the technology means that it can be trialled on surface contexts (e.g., skin and oral cancer) with no real potential for negative patient outcomes. Despite its potential to enable non-destructive assessment, ex vivo applications of multi and hyperspectral imaging dominate the field. Colon cancer stands out as cancer with relatively good in vivo accessibility that has not been investigated in this context. At the same time, we highlight brain tumours as cancer which, despite the comparative difficulty of accessing in vivo, would benefit greatly from a reduction in the clinical burdens created by the biopsy.

18640648, 0, Downloaded from https://onlinelibrary.wiley.com/doi/10.1002/jbio.202300105 by University of Adelaide Alumni, Wiley Online Library on [20/06/2023]. See the Terms and Conditions (https://onlinelibrary.wiley.com/terms-and-conditions) on Wiley Online Library for rules of use; OA articles are governed by the applicable Creative Commons License

Most studies, in vivo and ex vivo, used human clinical samples, with cell and animal models being relatively uncommon. Although this is an advantage to the field sample sizes were relatively low with studies positions as pilots of proofs-of-concept, and consequently little consideration was given to the generalisability of clinically meaningful comparisons (e.g. discriminating visibly suspicious lesions from fully healthy tissue). Additionally, many works limited themselves to identifying whether quantifiable differences in autofluorescence could be established, without investigating these characteristics' actual utility for cancer identification. Other studies which did investigate accuracy would have been improved by comparisons to current standard methods. Greater translational work is needed for this technology to achieve its potential.

Desirable optical characteristics for the non-invasive assessment of cells and tissues by hyperspectral imaging are highly specific to the intended application, with areas of functionality often laying in direct conflict with one another. Speed of image acquisition, for instance generally comes at the cost of image resolution and/or number of spectral channels assessed. Increasing the intensity of light used can mitigate this specific trade-off—enabling high-resolution images to be captured quickly—but this creates the potential for photobleaching and damage to sensitive tissues in vivo. High-sensitivity cameras for capturing emissions represent another mitigatory strategy, but their sensitivity applies equally to background light—difficult to control for in vivo, clinical applications—and they can be very costly with diminishing returns. Similarly, high magnification objectives can improve resolution without necessitating increased exposure times or higher intensity light, but are also expensive and give a more limited field of view, slowing data collection. However, with a considered focus on necessary characteristics, the process of optimisation can enable the development of hyperspectral devices able to perform their target function even under highly restrictive circumstances. A good example from outside of oncology is given by a series of works [67–73], where the development and validation of a hyperspectral catheter, able to generate real-time images inside of a beating to guide tissue ablation for the treatment of atrial fibrillation.

Two main technological strategies were observed; the application of one or very few excitation wavelengths with broad (often spectroscopic) assessment of emissions, and the use of a higher number of excitation wavelengths with a lower number of emission wavelengths assessed, often using wavelength-specific filters. Generally, the former was applied when specific fluorophores were being targeted as disease biomarkers and the latter was used when the intention was to develop a discriminatory spectral signature. Where the objective was tissue characterisation with real-time videography both excitation and emission wavelengths were constrained relative to other applications. The overwhelming focus has been on the discrimination of neoplastic tissue from normal tissue or suspicious but benign lesions. However, there is some indication that autofluorescence can indicate tumour characteristics, including metastatic potential [74] and drug response [75, 76], and future works should consider novel applications for the technology.

AUTHOR CONTRIBUTIONS

Jared M. Campbell, Ewa M. Goldys: Conceptualization. **Jared M. Campbell:** methodology. **Jared M. Campbell, Abbas Habibalahi, Shannon Handley, Saabah B. Mahbub, Ayad G. Anwer, Adnan Agha, and Ewa M. Goldys:** writing – original draft preparation. **Jared M. Campbell, Abbas Habibalahi, Shannon Handley, Saabah B. Mahbub, Ayad G. Anwer, Adnan Agha, and Ewa M. Goldys:** writing – review and editing. **Ewa M. Goldys, Jared M. Campbell:** supervision; **Ewa M. Goldys:** funding acquisition. All authors have read and agreed to the published version of the manuscript.

ACKNOWLEDGMENTS

Open access publishing facilitated by University of New South Wales, as part of the Wiley - University of New South Wales agreement via the Council of Australian University Librarians.

FUNDING INFORMATION

This research was funded by the Australian Research Council, grant number DP210102960 and a Cancer Institute NSW early career fellowship (2021/ECF1291).

CONFLICT OF INTEREST STATEMENT

The authors declare no conflict of interest. The funders had no role in the design of the study; in the collection, analyses, or interpretation of data; in the writing of the manuscript; or in the decision to publish the results.

DATA AVAILABILITY STATEMENT

Data sharing is not applicable to this article as no new data were created or analysed in this study.

ORCID

Jared M. Campbell https://orcid.org/0000-0003-0163-4251

REFERENCES

[1] D. Shin, S. S. Park, *World J. Gastrointest. Oncol.* **2013**, *5*, 4.
[2] M. L. Hinni, A. Ferlito, M. S. Brandwein-Gensler, R. P. Takes, C. E. Silver, W. H. Westra, et al., *Head Neck* **2013**, *35*, 1362.

18640648, 0, Downloaded from https://onlinelibrary.wiley.com/doi/10.1002/jbio.202300105 by University of Adelaide Alumni, Wiley Online Library on [20/06/2023]. See the Terms and Conditions (https://onlinelibrary.wiley.com/terms-and-conditions) on Wiley Online Library for rules of use; OA articles are governed by the applicable Creative Commons License

[3] M. Andreucci, R. Solomon, A. Tasanarong, *Biomed. Res. Int.* **2014**, *2014*, 741018.
[4] H. Duffau, *World Neurosurg.* **2014**, *81*, 56.
[5] T. J. Kaufmann, J. Huston 3rd., J. N. Mandrekar, C. D. Schleck, K. R. Thielen, D. F. Kallmes, *Radiology* **2007**, *243*, 812.
[6] J. M. Campbell, A. Habibalahi, S. Mahbub, M. Gosnell, A. G. Anwer, S. Paton, et al., *BMC Cancer* **2019**, *19*, 1242.
[7] S. B. Mahbub, A. Guller, J. M. Campbell, A. G. Anwer, M. E. Gosnell, G. Vesey, et al., *Sci. Rep.* **2019**, *9*, 4398.
[8] M. E. Gosnell, A. G. Anwer, J. C. Cassano, C. M. Sue, E. M. Goldys, *Biochim. Biophys. Acta* **2016**, *1863*, 56.
[9] G. A. Wagnieres, W. M. Star, B. C. Wilson, *Photochem. Photobiol.* **1998**, *68*, 603.
[10] T. S. Blacker, Z. F. Mann, J. E. Gale, M. Ziegler, A. J. Bain, G. Szabadkai, et al., *Nat. Commun.* **2014**, *5*, 3936.
[11] S. B. Mahbub, *Unsupervised hyperspectral unmixing analysis for label-free quantitative identification of native fluorophores in a biological sample by a robust dependent component analysis (RoDECA)*, Macquarie University, Sydney, Australia **2017**.
[12] A. U. Rehman, A. G. Anwer, M. E. Gosnell, S. B. Mahbub, G. Liu, E. M. Goldys, *Biomed. Opt. Express* **2017**, *8*, 1488.
[13] M. E. Gosnell, A. G. Anwer, S. B. Mahbub, S. Menon Perinchery, D. W. Inglis, P. P. Adhikary, et al., *Sci. Rep.* **2016**, *6*, 23453.
[14] C. Yang, V. W. Hou, E. J. Girard, L. Y. Nelson, E. J. Seibel, *J. Biomed. Opt.* **2014**, *19*, 76014.
[15] H. Duong, M. Han, *J. Neurosci. Methods* **2013**, *220*, 46.
[16] S. B. Mahbub, M. Ploschner, M. E. Gosnell, A. G. Anwer, E. M. Goldys, *Sci. Rep.* **2017**, *7*, 15792.
[17] A. Habibalahi, C. Bala, A. Allende, A. G. Anwer, E. M. Goldys, *Ocul. Surf.* **2019**, *17*, 540.
[18] A. Habibalahi, M. Dashtbani Moghari, J. M. Campbell, A. G. Anwer, S. B. Mahbub, M. Gosnell, et al., *Redox Biol.* **2020**, *34*, 1.
[19] Q. Li, X. He, Y. Wang, H. Liu, D. Xu, F. Guo, *J. Biomed. Opt.* **2013**, *18*, 100901.
[20] A. Habibalahi, A. Allende, C. Bala, A. G. Anwer, S. Mukhopadhyay, E. M. Goldys, *IEEE Access* **2019**, *7*, 141343.
[21] S. B. Mahbub, L. T. Nguyen, A. Habibalahi, J. M. Campbell, A. G. Anwer, U. M. Qadri, et al., *Sci. Rep.* **2021**, *11*, 1.
[22] A. Alfonso-Garcia, J. Bec, B. Weyers, M. Marsden, X. Zhou, C. Li, et al., *J. Biophotonics* **2021**, *14*, e202000472.
[23] R. Datta, A. Gillette, M. Stefely, M. C. Skala, *J. Biomed. Opt.* **2021**, *26*, 1.
[24] Y. Pu, W. Wang, Y. Yang, R. R. Alfano, *Appl. Optics* **2013**, *52*, 1293.
[25] T. Dramicanin, L. Lenhardt, I. Zekovic, M. Dramicanin, *J. Res. Phys.* **2013**, *36*, 53.
[26] S. Kwon, W. Yang, D. Moon, K. S. Kim, *J. Cancer* **2020**, *11*, 5403.
[27] S. Madhuri, N. Vengadesan, P. Aruna, D. Koteeswaran, P. Venkatesan, S. Ganesan, *Photochem. Photobiol.* **2003**, *78*, 197.
[28] M. M. Lukina, M. V. Shirmanova, T. F. Sergeeva, E. V. Zagaynova, *Sovrem. Tehnol. Med.* **2016**, *8*, 113.
[29] T. Le Bourgeois, L. Strauss, H. I. Aksoylar, S. Daneshmandi, P. Seth, N. Patsoukis, et al., *Front. Oncol.* **2018**, *8*, 237.
[30] M. Wang, F. Long, F. Tang, Y. Jing, X. Wang, L. Yao, et al., *Appl. Sci.* **2017**, *7*, 32.
[31] G. Fenhalls, M. Geyp, D. M. Dent, M. I. Parker, *Br. J. Cancer* **1999**, *81*, 1142.
[32] K. Pandey, A. Pradhan, A. Agarwal, A. Bhagoliwal, N. Agarwal, *J. Obstet. Gynaecol. India* **2012**, *62*, 432.
[33] L. Zhang, Y. Pu, J. Xue, S. Pratavieira, B. Xu, S. Achilefu, et al., *J. Biomed. Opt.* **2014**, *19*, 37005.
[34] M. D. Peters, C. M. Godfrey, H. Khalil, P. McInerney, D. Parker, C. B. Soares, *Int. J. Evid. Based Healthc.* **2015**, *13*, 141.
[35] J. Deal, S. Mayes, C. Browning, S. Hill, P. Rider, C. Boudreaux, et al., *J. Biomed. Opt.* **2018**, *24*, 1.
[36] B. Banerjee, N. S. Rial, T. Renkoski, L. R. Graves, S. A. Reid, C. Hu, et al., *Lasers Surg. Med.* **2013**, *45*, 573.
[37] B. Banerjee, T. Renkoski, L. R. Graves, N. S. Rial, V. L. Tsikitis, V. Nfonsam, et al., *J. Biomed. Opt.* **2012**, *17*, 016003.
[38] B. O. Meyer, M. P. Stella, B. Holst, B. Nielsen, K. Holmstrom, P. Andersen, et al., *J. Biomed. Opt.* **2020**, *25*, 1.
[39] J. Kim, H. M. Lew, J. H. Kim, S. Youn, H. A. Faruque, A. N. Seo, et al., *IEEE Trans. Med. Imaging* **2021**, *40*, 594.
[40] D. Roblyer, C. Kurachi, V. Stepanek, R. A. Schwarz, M. D. Williams, A. K. El-Naggar, et al., *J. Biomed. Opt.* **2010**, *15*, 066017.
[41] J. A. Jo, S. Cheng, R. Cuenca-Martinez, E. Duran-Sierra, B. Malik, B. Ahmed, et al., *Annu. Int. Conf. IEEE Eng. Med. Biol. Soc.* **2018**, *2018*, 3009.
[42] G. Lu, D. Wang, X. Qin, S. Muller, X. Wang, A. Y. Chen, et al., *J. Biophotonics* **2018**, *11*, 1.
[43] R. Pal, K. Edward, L. Ma, S. Qiu, G. Vargas, *Lasers Surg. Med.* **2017**, *49*, 866.
[44] E. Duran-Sierra, S. Cheng, R. Cuenca-Martinez, B. Malik, K. C. Maitland, Y. S. Lisa Cheng, et al., *Oral Oncol.* **2020**, *105*, 104635.
[45] N. Bedard, R. A. Schwarz, A. Hu, V. Bhattar, J. Howe, M. D. Williams, et al., *Biomed. Opt. Express* **2013**, *4*, 938.
[46] Y. J. Yan, T. W. Huang, N. L. Cheng, Y. F. Hsieh, M. H. Tsai, J. C. Chiou, et al., *J. Biomed. Opt.* **2017**, *22*, 1.
[47] Y. J. Yan, N. L. Cheng, C. I. Jan, M. H. Tsai, J. C. Chiou, M. Ou-Yang, *Sensors* **2021**, *21*, 1.
[48] J. R. Duann, C. I. Jan, M. Ou-Yang, C. Y. Lin, J. F. Mo, Y. J. Lin, et al., *J. Biomed. Opt.* **2013**, *18*, 126005.
[49] M. Halicek, J. D. Dormer, J. V. Little, A. Y. Chen, B. Fei, *Biomed. Opt. Express* **2020**, *11*, 1383.
[50] M. Halicek, J. D. Dormer, J. V. Little, A. Y. Chen, L. Myers, B. D. Sumer, et al., *Cancers* **2019**, *11*, 1.
[51] A. T. Shah, M. C. Skala, in *Multiphoton microscopy in the biomedical sciences XV* (Eds: A. Periasamy, P. T. C. So, K. König), International Society for Optics and Photonics, Bellingham, WA **2015**.
[52] B. Fei, L. Guolan, M. T. Halicek, X. Wang, H. Zhang, J. V. Little, et al., *Annu. Int. Conf. IEEE Eng. Med. Biol. Soc.* **2017**, *2017*, 4041.
[53] G. Lu, J. V. Little, X. Wang, H. Zhang, M. R. Patel, C. C. Griffith, et al., *Clin. Cancer Res.* **2017**, *23*, 5426.
[54] R. A. Romano, R. G. Teixeira Rosa, A. G. Salvio, J. A. Jo, C. Kurachi, *Photodiagnosis Photodyn. Ther.* **2020**, *101704*, 1.
[55] A. Lihachev, A. Derjabo, I. Ferulova, M. Lange, I. Lihacova, J. Spigulis, *J. Biomed. Opt.* **2015**, *20*, 120502.
[56] G. E. Carver, S. A. Locknar, D. L. Weaver, J. L. Stein, G. S. Stein, *J. Cell. Physiol.* **2019**, *234*, 5413.
[57] M. D. Keller, S. K. Majumder, M. C. Kelley, I. M. Meszoely, F. I. Boulos, G. M. Olivares, et al., *Lasers Surg. Med.* **2010**, *42*, 15.
[58] S. J. Bae, D. S. Lee, V. Berezin, U. Kang, K. H. Lee, *J. Obstet. Gynaecol. Res.* **2016**, *42*, 1846.

18640648, 0, Downloaded from https://onlinelibrary.wiley.com/doi/10.1002/jbio.202300105 by University of Adelaide Alumni, Wiley Online Library on [20/06/2023]. See the Terms and Conditions (https://onlinelibrary.wiley.com/terms-and-conditions) on Wiley Online Library for rules of use; OA articles are governed by the applicable Creative Commons License

[59] Y. Li, X. Xie, X. Yang, L. Guo, Z. Liu, X. Zhao, et al., *J. Biophotonics* **2019**, *12*, e201800324.
[60] B. Pradère, F. Poulon, E. Compérat, I. T. Lucas, D. Bazin, S. Doizi, et al., *J. Biophotonics* **2018**, *11*, 1.
[61] V. Kilin, C. Mas, S. Constant, J. P. Wolf, L. Bonacina, *Sci. Rep.* **2017**, *7*, 1.
[62] F. Poulon, A. Chalumeau, F. Jamme, J. Pallud, P. Varlet, H. Mehidine, et al., *Front. Phys.* **2018**, *6*, 109.
[63] F. Poulon, J. Pallud, P. Varlet, M. Zanello, F. Chretien, E. Dezamis, et al., *Sci. Rep.* **2018**, *8*, 1.
[64] T. E. Renkoski, K. D. Hatch, U. Utzinger, *J. Biomed. Opt.* **2012**, *17*, 036003.
[65] A. J. Schupper, M. Rao, N. Mohammadi, R. Baron, J. Y. K. Lee, F. Acerbi, et al., *Front. Neurol.* **2021**, *12*, 682151.
[66] A. Habibalahi, A. Allende, J. Michael, A. G. Anwer, J. Campbell, S. B. Mahbub, et al., *Cancers* **2022**, *14*, 1.
[67] L. M. Swift, H. Asfour, N. Muselimyan, C. Larson, K. Armstrong, N. A. Sarvazyan, *Heart Rhythm* **2018**, *15*, 564.
[68] S. Guan, H. Asfour, N. Sarvazyan, M. Loew, *J. Med. Imaging* **2018**, *5*, 046003.
[69] H. Asfour, S. Guan, N. Muselimyan, L. Swift, M. Loew, N. Sarvazyan, *Biomed. Opt. Express* **2018**, *9*, 2189.
[70] D. A. Gil, L. M. Swift, H. Asfour, N. Muselimyan, M. A. Mercader, N. A. Sarvazyan, *J. Biophotonics* **2017**, *10*, 1008.
[71] N. Muselimyan, L. M. Swift, H. Asfour, T. Chahbazian, R. Mazhari, M. A. Mercader, et al., *PLoS One* **2016**, *11*, e0167760.
[72] K. Armstrong, C. Larson, H. Asfour, T. Ransbury, N. Sarvazyan, *Cardiovasc. Eng. Technol.* **2020**, *11*, 560.
[73] N. Muselimyan, H. Asfour, N. Sarvazyan, *Sci. Rep.* **2020**, *10*, 1.
[74] K. Alhallak, L. G. Rebello, T. J. Muldoon, K. P. Quinn, N. Rajaram, *Biomed. Opt. Express* **2016**, *7*, 4364.
[75] T. M. Cannon, A. T. Shah, M. C. Skala, *Biomed. Opt. Express* **2017**, *8*, 1911.
[76] A. T. Shah, K. E. Diggins, A. J. Walsh, J. M. Irish, M. C. Skala, *Neoplasia* **2015**, *17*, 862.

How to cite this article: J. M. Campbell, A. Habibalahi, S. Handley, A. Agha, S. B. Mahbub, A. G. Anwer, E. M. Goldys, *J. Biophotonics* **2023**, e202300105. https://doi.org/10.1002/jbio.202300105

18640648, 0, Downloaded from https://onlinelibrary.wiley.com/doi/10.1002/jbio.202300105 by University of Adelaide Alumni, Wiley Online Library on [20/06/2023]. See the Terms and Conditions (https://onlinelibrary.wiley.com/terms-and-conditions) on Wiley Online Library for rules of use; OA articles are governed by the applicable Creative Commons License